ELSEVIER

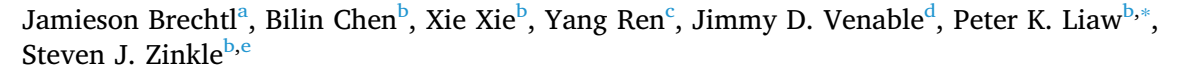
Contents lists available at ScienceDirect

Materials Science & Engineering A

journal homepage: www.elsevier.com/locate/msea



Entropy modeling on serrated flows in carburized steels





b Department of Materials Science and Engineering, The University of Tennessee, Knoxville, TN, 37996, USA

ARTICLE INFO

Keywords: Stress/strain measurements Modeling/simulations Hardness Iron alloys Plasticity

ABSTRACT

Samples comprised of carburized steel alloys, 4615, 4720, and 10B22, were tension tested at room temperature and at a strain rate of $2\times 10^{-4}~\rm s^{-1}$. The serrated-flow behavior was modeled and analyzed, using the refined composite multiscale entropy (RCMSE) method. High energy X-ray diffraction revealed the body-centered-cubic (BCC) structure of the three alloys in the as-received condition. Moreover, Vickers-hardness experiments were performed, which showed an increase in the hardness of the alloy that corresponded to increasing impurity concentrations. Here the diffusion coefficient of carbon in the three alloys were estimated, respectively, to be $2.5\times 10^{-11}~\rm m^2/s$, $5.1\times 10^{-11}~\rm m^2/s$, and $2.8\times 10^{-11}~\rm m^2/s$ for alloys, 10B22, 4615, and 4720, respectively, which agree with the values found in the literature for α -iron. Moreover, the sample entropy, on average, increased with respect to the heating time, and, consequently, the amount of carbon that had diffused into the alloy. The above results show that the complexity of the serration behavior in the alloys studied increases with respect to the amount of carbon that has diffused into the material.

1. Introduction

A serrated flow, which occurs during the plastic regime following the yield point, is typically identified as oscillations in the stress vs. strain curve. Furthermore, this kind of behavior is non-linear in nature and occurs in various alloys, including metallic glasses [1–16], high entropy alloys [14,17–30], and various other material systems [14,31–50]. Importantly, serrations can exhibit complex dynamics across multiple time scales. This complexity, which is related to the degree of regularity of a given time series, can be quantified on different time scales.

In the past, several methods have been employed to gauge the complex behavior of a given set of temporal data [51]. One method that can analyze this type of phenomenon is known as the multiscale entropy (MSE) algorithm, which was proposed as a technique to overcome the limitations of the traditional entropy-based algorithms [52]. The MSE algorithm consists of a two-step process where the first step involves a coarse-graining procedure that is used to characterize the dynamics of a given system across multiple time scales [53].

The MSE algorithm is then utilized, for a given time scale, to evaluate the complexity of the corresponding coarse-grained time series.

The resulting quantity, which gauges the degree of complexity in the time series, is known as the sample entropy (SE) [54]. For a given time series, higher SE values typically signify a more irregular data set. In contrast, a time series that is more predictable is usually characterized by lower values. As discussed by Costa et al. [55], this algorithm estimates the likelihood that two sequences of m consecutive data points, which are similar, will remain comparable when an additional consecutive point is included.

Costa et al. found that the MSE algorithm could resolve the issue of lower entropy values of the 1/f noise (f is the frequency of the generated noise), as compared to the white noise, despite the former being more complex in nature [52,56]. Moreover, their study employed the MSE algorithm to differentiate the heart-rate time series among healthy, atrial fibrillation, and congestive heart-failure subjects. In recent years, the MSE algorithm has been used in many studies to model and analyze various phenomena, including biological signals, financial-time series, and serrated-flow behavior during mechanical testing [31,52,54,57]. However, there are still issues with the implementation of the MSE technique. For example, a data set that is relatively small (N < 750) may lead to an inaccurate estimation and even undefined results [56].

E-mail address: pliaw@utk.edu (P.K. Liaw).

^cX-ray Science Division, Argonne National Laboratory, Argonne, IL, 60439, USA

^d Columbus McKinnon, Lexington, TN, 38351, USA

^e Department of Nuclear Engineering, The University of Tennessee, Knoxville, TN, 37996, USA

^{*} Corresponding author.

Wu et al. developed the composite multiscale entropy, and later the refined composite multiscale entropy (RCMSE) algorithm to address the issues that were associated with the accuracy of the MSE algorithm [53,54]. The advantage of the RCMSE algorithm over the MSE method is that it can be used to increase the accuracy of the entropy estimation in addition to reducing the probability of inducing the undefined entropy when modeling and analyzing short-time series [54]. However, there is a greater computational cost for the RCMSE, as compared to the MSE algorithm. To date, the RCMSE method has been applied to study the serrated flow, chaos, noise, and small-world networks [30,56,58,73].

Sarkar et al. analyzed and compared the complexity of serrations exhibited in a substitutional and interstitial alloy using the MSE algorithm [31]. Here the substitutional alloy consisted of an Al-Mg2.5 weight percent (wt.%) alloy while the interstitial alloy was a lowcarbon steel. It was found that the low-carbon steel exhibited significantly-larger sample-entropy values during the serrated flow than the Al-Mg alloy. According to Sarkar et al., a couple of factors may have led to the differences in the complexity exhibited by the alloys. In the Al-Mg alloy, the size mismatch between the host (Al) and the solute (Mg) is $\sim 12\%$, which is relatively high [31]. Because of the sphericallysymmetric size-misfit effect, the solute atoms primarily interact with only the edge dislocations in the matrix. With respect to the steel alloy, carbon atoms produce tetragonal distortions at octahedral sites, which can interact with both edge and screw dislocations [31,59]. Moreover, carbon atoms on the octahedral sites can accumulate around a screw dislocation twice as much as an edge dislocation [60]. This greater variety of interactions in the steel during the serrated flow, therefore, is what leads to the stress-drop behavior, which is more complex in nature.

Currently, there are few studies that examine how the concentration of impurities affects the complexity of the serration behavior in steels undergoing tension tests. Therefore, this paper will examine the critical issue of how the carbon content affects the complexity of serrated flows in low-carbon steel alloys, via the RCMSE technique. In doing so, it is hoped that the present work will advance our fundamental understanding as to how impurities can affect the dynamics of the serration behavior in steels.

2. Materials and methods

The low-carbon steel samples, 10B22, 4615, and 4720 (Table 1 gives their actual chemical compositions), were machined from steel wires (see Fig. 1 for the sample geometry). As can be seen, the composition of the as-cast 10B22 steel alloy in wt.% was: 0.22%C, 0.95% Mn, 0.009%P, 0.009%S, 0.250%Si, 0.04%Ni, 0.06%Cr, 0.01%Mo, 0.09%Cu, 0.006%Sn, 0.001%V, 0.036%Al, 0.0050%N, 0.0023%B, 0.021%Ti, and 0.001%Nb. Furthermore, the composition of the as-cast 4615 steel alloy was: 0.13–0.18%C, 0.45–0.65%Mn, 0.035%P (max.), 0.040%S (max.), 0.15–0.35%Si, 1.65–2.0%Ni, and 0.20–0.30%Mo. While the composition of the as-cast 4720 alloy was: 0.17–0.22%C, 0.50–0.70%Mn, 0.035%P (max.), 0.040%S (max.), 0.15–0.35%Si, 0.90–1.20%Ni, 0.35–0.55%Cr, and 0.15–0.25%Mo. As evident in Table 1, the nickel and molybdenum concentrations were the highest for the alloy, 4615, and the lowest for 10B22 in the as-received state. Moreover, the manganese content was the highest in the alloy, 4720,

and the lowest in the alloy, 10B22.

After fabrication, the specimens were heat treated at a temperature of 885 °C in an environment containing CO, CO₂, CH₄, and N₂ gas with a potential carbon concentration of 0.7 (volume percent). The exposure time for the samples at the above temperature were 30, 45, 60, and 70 min. To ensure that the carbon concentration remained at an optimal level, the amount of the natural gas in the system was constantly monitored and adjusted. After the carburization, the samples were quenched in oil and rinsed with the pressurized, high-temperature water. Specimens were, then, tempered by placing them into another furnace and heating them in air at 260 °C for 3 h. After tempering, the samples were air cooled.

To identify the crystalline structures of these steels, high-energy X-ray diffraction (XRD) was performed at the 11-ID-C beam-line located in the Advanced Photon Source (APS) at Argonne National Laboratory. For the diffraction, the wavelength of the X-ray was 0.117 Å, and the beam energy was $\sim\!115\,\text{keV}.$ Additionally, polished samples with a thickness of 1.5 mm were used in the experiments. Diffraction patterns were captured at different locations near the center of the sample, and the results were compared to minimize the error of the patterns.

Uniaxial tension experiments were performed, using an 810 Material Test System (MTS) machine. The tests were conducted at room temperature with a strain rate of $2\times 10^{-4}\,{\rm s}^{-1}$ until fracture. For the data acquisition, a rate of 100 Hz was used. To remove the trend in the data caused by necking, a moving average fit of the stress vs. time data was performed and, then, subracted from the curve. After the tension tests, the fracture surfaces were examined, using scanning-electron microscopy (SEM, Carl Zeiss, Oberkochen, Germany). This device employed a LEO Gemini 1525 field-emission scanning-electron microscope equipped with the backscattering-electron (BSE, K. E. Developments Ltd., Cambridge, UK) detector. An electron high tension (EHT) voltage value of 20 kV was used for imaging.

To gauge the carbon migration in the steel alloys, Vickers-hardness experiments were performed (Buehler Instron Tukon 1102). Here, the hardness was measured as a function of case depth, where 12 indents were taken at depths ranging from $\sim\!50$ to 2,000 μ m in the axial direction. Specimen preparation involved cutting the end section of a sample in the transverse direction, which was subsequently ground and polished to a mirror finish. For the indentations, a load of 100 gf (gram force) and a dwell time of 15 s were used in which the indents were made in accordance with the American Society for Testing and Materials (ASTM) E384-16 standards [61].

3. Analytical methods

3.1. Refined composite multiscale entropy algorithm

To begin studying the complexity of the time series, the stress vs. time curve is first normalized by subtracting away the moving average or polynomial fit of the time-series data [33]. From the resultant data set, one generates the coarse-grained time series, $y_{k,j}^{\tau}$, via the following equation:

$$y_{k,j}^{\tau} = \frac{1}{\tau} \sum_{i=(j-1)\tau+k}^{j\tau+k-1} x_i \; ; \; 1 \le j \le \frac{N}{\tau} \; ; \; 1 \le k \le \tau$$
 (1)

Table 1
Actual chemical compositions (in wt.%) of steel alloys, 10B22, 4615, and 4720.

10B22	С	Mn	P	S	Si	Ni	Cr	Mo
	0.22	0.95	0.009	0.009	0.250	0.04	0.06	0.01
	Cu	Sn	V	Al	N	В	Ti	Nb
	0.09	0.006	0.001	0.036	0.0050	0.0023	0.021	0.001
	С	Mn	P(max.)	S(max.)	Si	Ni	Cr	Mo
4615	0.13-0.18	0.45-0.65	0.035	0.040	0.15-0.35	1.65-2.0	-	0.20-0.30
4720	0.17-0.22	0.50-0.70	0.035	0.040	0.15-0.35	0.90-1.20	0.35-0.55	0.15-0.25

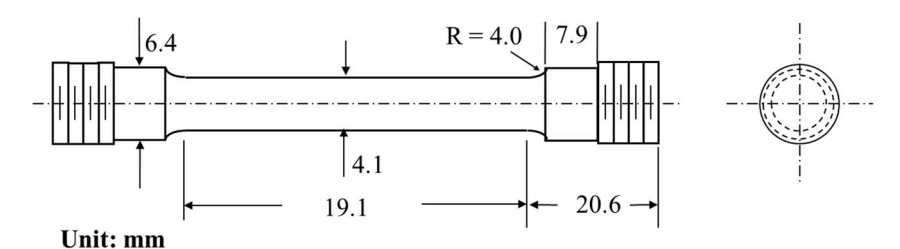


Fig. 1. Specimen geometry for the tension test.

where τ is the scale factor, x_i is a value from the initial data set, and k represents an index that determines on which x_i the coarse-graining procedure is initialized. Moreover, the scale factor is an averaged factor, which determines the length of the coarse-grained time series. A schematic of Eq. (1) can be seen in Fig. 2. Using the terms evaluated from the above equation, one makes the template vectors, $y_{k,i}^{\tau,m}$, of the dimension (or size), m [53]:

$$y_{k,i}^{\tau,m} = \{ y_{k,i}^{\tau} \ y_{k,i+1}^{\tau} \ \dots \ y_{k,i+m-1}^{\tau} \} ; \ 1 \le i \le N-m ; \ 1 \le k \le \tau$$
 (2)

here $y_{k,i}^{\tau}$ is simply the ith component of the vector and is the quantity as defined from Eq. (1). After the template vectors are determined, one calculates the number, n, of matching sets of distinguishable template vectors. To determine whether two distinct vectors match, the infinity norm, d, of the difference between them, is calculated from the following relation [62]:

$$d_{ab}^{\tau,m} = ||\mathbf{y}_{\mathbf{a}}^{\tau,\mathbf{m}} - \mathbf{y}_{\mathbf{b}}^{\tau,\mathbf{m}}||_{\infty} = \max\{|y_{1,a}^{\tau} - y_{1,b}^{\tau}| \dots |y_{i+m-1,a}^{\tau} - y_{i+m-1,b}^{\tau}|\} < r$$
(3)

where r is a tolerance value that is predefined, a and b are the indices of some chosen vector, y, as given in Eq. (2), where $a \neq b$. According to Refs. [52,54,56,63], m=2, and r is typically set as $0.15 \times \sigma$ (σ is the standard deviation of the relevant data) to reduce the standard error in the sample entropy results. After the number of matching vectors is calculated, this method is performed again for $y_{k,i}^{\tau,m+1}$. Once the total number of matching vectors, n_k^m and n_k^{m+1} , are found, they are summed for k=1 to τ . Next, the RCMSE value of the data set for a given scale is calculated, using the following equation [64]:

$$RCMSE(y, \tau, m, r) = Ln\left(\frac{\sum_{k=1}^{\tau} n_{k,\tau}^{m}}{\sum_{k=1}^{\tau} n_{k,\tau}^{m+1}}\right)$$
(4)

To gain a basic understanding of how the RCMSE algorithm works, the colored noise was modeled and analyzed. Using a similar method as that employed in Ref. [52], 2×10^2 sets of white noise signals (10^4 data points each) were produced. The fast Fourier transform was then applied to the resulting data, which yielded a power spectrum that was subsequently filtered to behave as a $1/f^{\alpha}$ distribution. Then, the distribution was inverse-Fourier transformed. Here, α is the power-spectrum exponent, which describes the power-law behavior of the distribution. This process was accomplished for $\alpha = -2$, -1, 0, 1, and 2, which, respectively, yielded data for the violet, blue, white, pink, and brown noise.

A plot of the sample entropy (sample en.) for the noise described above can be seen in Fig. 3. Here, each curve displays the monotonic behavior with an increase in the scale factor. The complexity values for the colored noise with power-spectrum exponents, 1, 0, - 1, and - 2, obey strictly decreasing trends while the brown noise ($\alpha=2$) increased with respect to the scale factor. Results from the analysis show that the pink noise in general corresponds to higher sample entropy values, relative to the other types of colored noise. This result further supports the idea that the 1/f noise possesses long-range correlations that are the most complex in nature [54,56].

4. Results

4.1. Complexity modeling and analysis

Fig. 4 shows the SEM image of the fractured surface of the alloy, 10B22, that was heated for 70 min. prior to tension testing. It should be noted that all three alloys possessed similar fracture surfaces. As can be seen, the surface contains microvoid coalescence that is interspersed across the entire region. Furthermore, fracture surfaces exhibited a cupand-cone geometry. The above results indicate that the alloys underwent the ductile fracture during tension. Fig. 5 presents the synchrotron X-ray diffraction patterns of the as-received samples, 10B22, 4615, and 4720. As can be seen in the graph, the peaks reveal that the samples contain a simple body-centered-cubic (BCC) structure.

Table 2 presents the uniform and total strains for the alloys under all annealing conditions. Here, the uniform strain is defined as the elongation at the maximum load, while the total strain is the elongation of the sample at fracture. As can be seen, the alloy, 4615, on average, exhibited the smallest uniform elongation and largest total elongation, as compared to the other alloys. In contrast, the alloy, 4720, displayed the greatest uniform elongation in the series. In addition, the lowest total strain was observed in the alloy 10B22 specimen that was heated for 30 min.

Fig. 6(a)-(c) display the engineering stress vs. strain curves for alloys, 10B22, 4615, and 4720. As can be seen, the alloys reach a maximum stress value and then undergo necking, where the serrated flow occurs. For all the cases, the stress drops were found to occur below the general level of the flow curve, which is indicative of Type-C serrations [14,65]. Fig. 7(a)-(c) present the graphs of the engineering stress vs. time curves for all three alloys. Like in Fig. 6(a)-(c), it can be observed that the stress curve is smooth until the alloy undergoes necking, where the serrated type of deformation occurs. In contrast to the serrations that were observed in the previous figures, these fluctuations exhibit a wavy characteristic, which occurs until failure. Moreover, the fluctuations appear to be increasing in magnitude with respect to time.

The results of the RCMSE analysis are displayed in Fig. 8(a)-(c). These results were based on data that was taken from the necking regime and adjusted, relative to the moving average [33]. Interestingly, the complexity increased with respect to the scale factor, indicating that the serrated-like flow exhibited complexity at all scales. Furthermore, the sample entropy generally increased with increasing the heating time of the alloy. It should be noted that in the alloy, 4615, the largest sample-entropy curve was exhibited in the material heated for 60 min. Furthermore, the 60 and 70 min. curves in the alloy, 4720, are approximately the same for scale factors \leq 13, after which the curve for 60 min. attains larger values.

4.2. Vickers-hardness tests

Fig. 9(a)-(c) show the Vickers hardness as a function of the case depth for each alloy. Here the hardness decreased as a function of the case depth. Furthermore, the hardness curves had a general increase with respect to the heating time. From the hardness results, the diffusion coefficient of carbon could be estimated, using the following

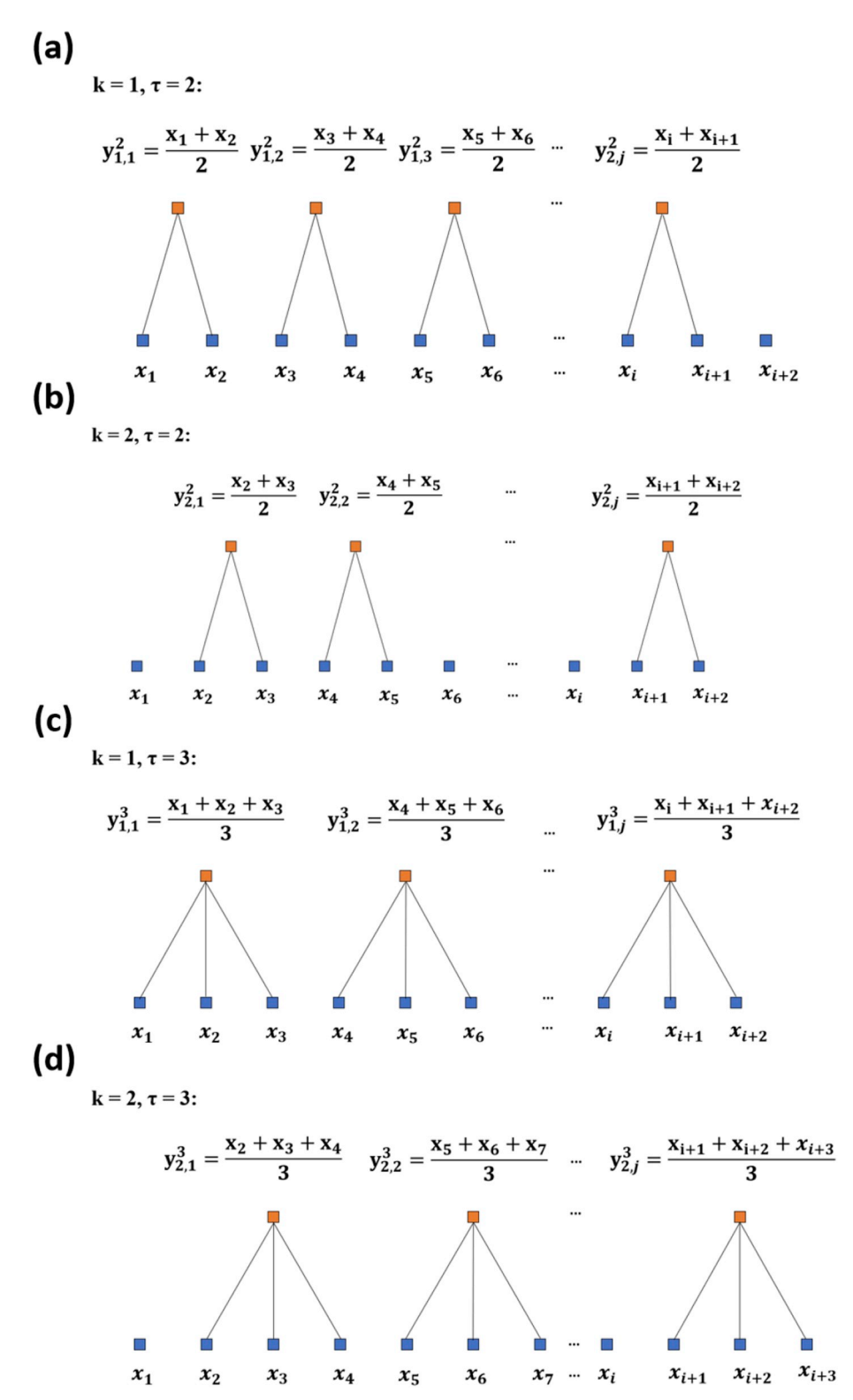


Fig. 2. Visual representation of the coarse-graining procedure for (a) k = 1, $\tau = 2$, (b) k = 1, $\tau = 3$, (c) k = 2, $\tau = 2$, and (d) k = 2, $\tau = 3$ [56].

equation [66]:

$$H(x) = H_0 + (H_{max} - H_0)erfc\left(\frac{x}{2\sqrt{Dt}}\right)$$
(5)

here x, H_{max} , H_{0} , D, and t are, respectively, the case depth, bulk hardness (hardness at the largest case depth value), near-surface hardness ($x \sim 50 \, \mu \text{m}$), diffusion coefficient in m^2/s , and heating time in seconds. To estimate the diffusion coefficient, Dt was first algebraically solved

[see Eq. (6)] using Eq. (5) and, then, plotted with respect to the heating time (in minutes).

$$Dt = \frac{x_{1/2}^{2}}{4\left[erfc^{-1}\left(\frac{H_{1/2} - H_{0}}{H_{max} - H_{0}}\right)\right]^{2}}$$
(6)

 $H_{1/2}$ and $x_{1/2}$ are, respectively, the hardness and case depth at half the hardness saturation point. Fig. 10(a)–(c) show the plot of the right-hand

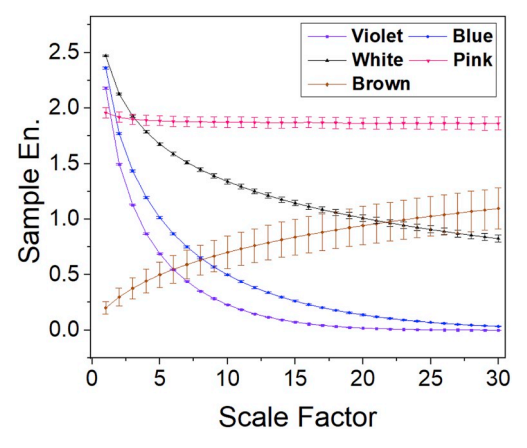


Fig. 3. Sample-entropy curves for violet, blue, white, pink, and brown noise.

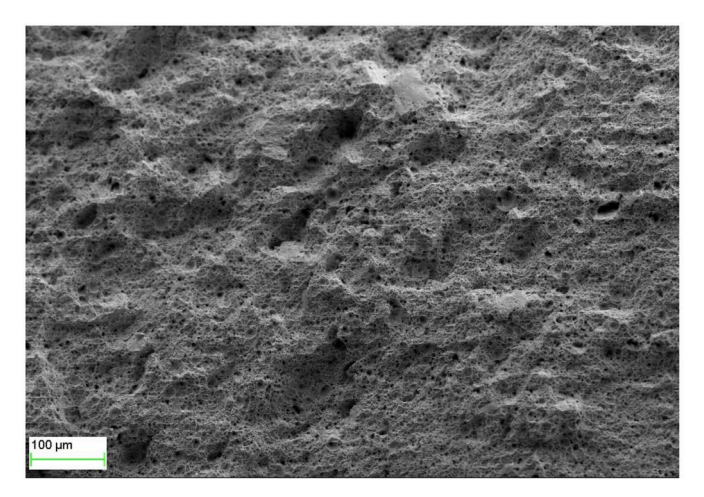


Fig. 4. Fracture surface of the carburized steel alloy, 10B22, after tensile testing at a strain rate of 2×10^{-4} s⁻¹.

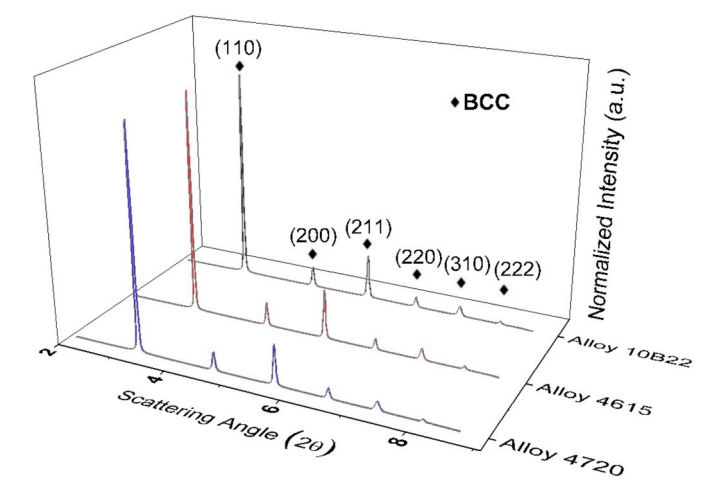


Fig. 5. X-ray diffraction results for the as-received alloys, 10B22, 4615, and 4720.

side of Eq. (6) as a function of heating time. From the data, the slope was fit in which D was estimated to be approximately $2.5 \times 10^{-11} \, \text{m}^2/\text{s}$, $5.1 \times 10^{-11} \, \text{m}^2/\text{s}$, and $2.8 \times 10^{-11} \, \text{m}^2/\text{s}$ for the alloys, 10B22, 4615, and 4720, respectively. The above values appear to be in agreement with the range of values listed in Ref. [67] for α -iron ($2.4 \times 10^{-12} - 1.7 \times 10^{-10} \, \text{m}^2/\text{s}$).

To compare the relative complexity of the time series for each alloy,

Table 2Uniform and total strains for alloys, 10B22, 4615, and 4720, annealed at 885 °C for 30, 45, 60, and 70 min., respectively.

Alloy	Annealing Time (min.)	Uniform Strain (%)	Total Strain (%)
10B22	30	5.1	10.7
	45	5.8	13.5
	60	5.6	13.1
	70	5.4	13.0
4615	30	4.7	13.4
	45	5.2	14.1
	60	5.3	13.6
	70	5.2	13.2
4720	30	5.9	13.3
	45	5.2	12.8
	60	6.1	13.6
	70	6.0	11.9

the area enclosed under the RCMSE curve (denoted A_{SE}) was calculated for each annealing condition. These values were then plotted with respect to the average diffusion distance of $\langle x \rangle = \sqrt{2Dt}$, as displayed in Fig. 11(a)-(c). Here, a greater area is indicative of a time series that is more complex [68]. As can be seen from the graph, there is a linear correlation between the average distance that the carbon has diffused, and the complexity of the serrated type flow. This result provides the evidence that as the carbon content is increased in the alloy, the corresponding serrated flow is involved in more complex dynamics.

Fig. 12 presents a combined graph of A_{SE} vs. < x > for all three alloys. Based on Table 1, it is apparent in the graphs that the representative curves shift to the right as the initial carbon concentration in the as-received state of the alloy decreases. Moreover, for heating times of 30 and 45 mins., the value A_{SE} was greater for alloys 4615 and 4720, where both alloys had a lower initial carbon concentration as compared to alloy 10B22. Finally, the curve for the alloy, 4615, had the most significant changes in the average diffusion distance and average complexity for heating times < 70 min.

5. Discussion

5.1. Effects of microstructure on mechanical behavior

During fabrication, carbon atoms settle into octahedral sites in the body-centered-cubic (BCC) lattice along perpendicular orientations, as the steel is cooled to ambient temperature [69]. As the steel undergoes the tension strain, the interstitial carbon atoms react by hopping to adjacent octahedral sites, which are on the lattice edge parallel to the associated stress. In other words, the applied stress favors atoms, which are arranged in sites that have tetragonality and match the lattice strains imposed by the interstitials. This type of interstitial reordering under an applied stress is known as Snoek ordering [59,70]. Interestingly, this type of rearrangement is a mechanism, which plays a role in the repeated yielding of low-carbon steels [71].

A second mechanism that leads to yielding also involves interstitial atoms that have settled into octahedral sites. At the octahedral sites, the atoms create tetragonal distortions that can interact with both screw and edge dislocations. Moreover, the carbon atoms can also interact twice as much with a screw dislocation than with an edge dislocation [31]. When combined, these two factors can lead to an increase in the variety of interactions, which may take place during the serrated flow in the steel

Fig. 9(a)-(c) present the Vickers hardness of the steel alloys, where the values increased gradually with respect to the heating time. The rise in hardness is most likely due to the increased amount of carbon that has diffused into the matrix. This trend is corroborated by the fact that the estimated root-mean squares displacement showed that carbon, on average, diffused further into the sample as the heating time increased [see Fig. 10(a)-(c)]. An increase in the carbon concentration, in theory,

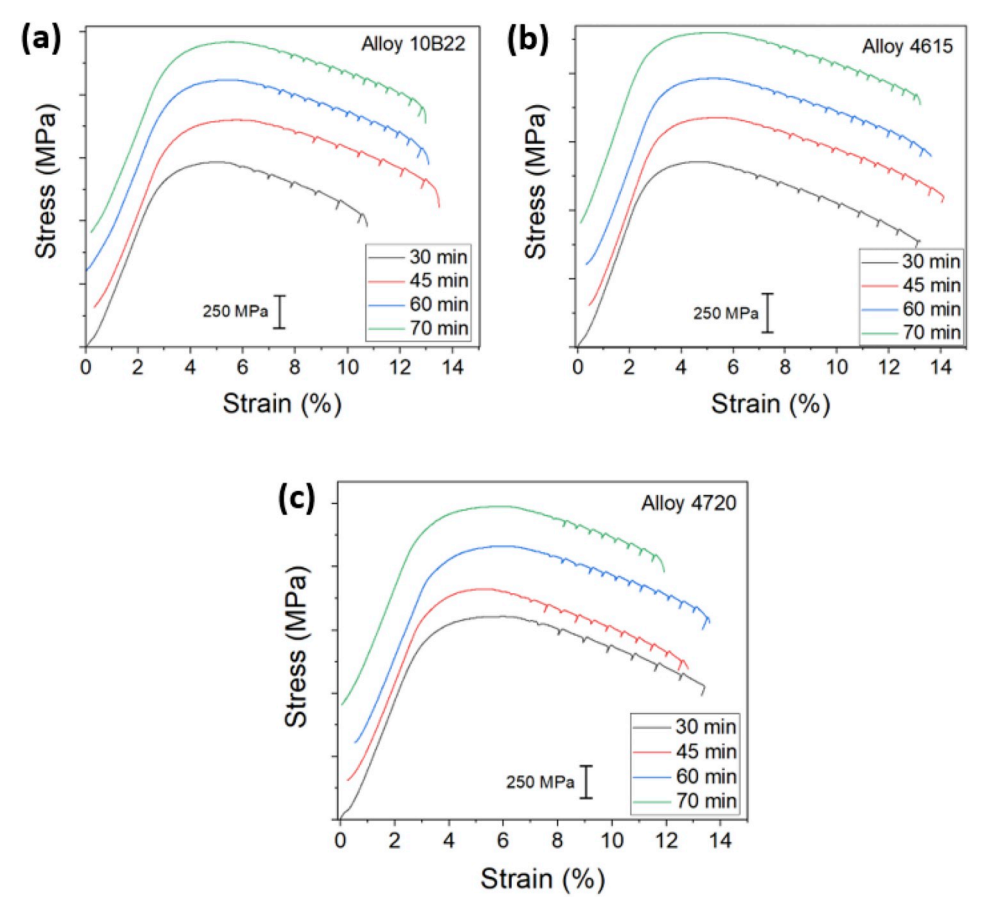


Fig. 6. Engineering stress vs. strain graphs. Here serrations can be observed for alloys, (a) 10B22, (b) 4615, and (c) 4720.

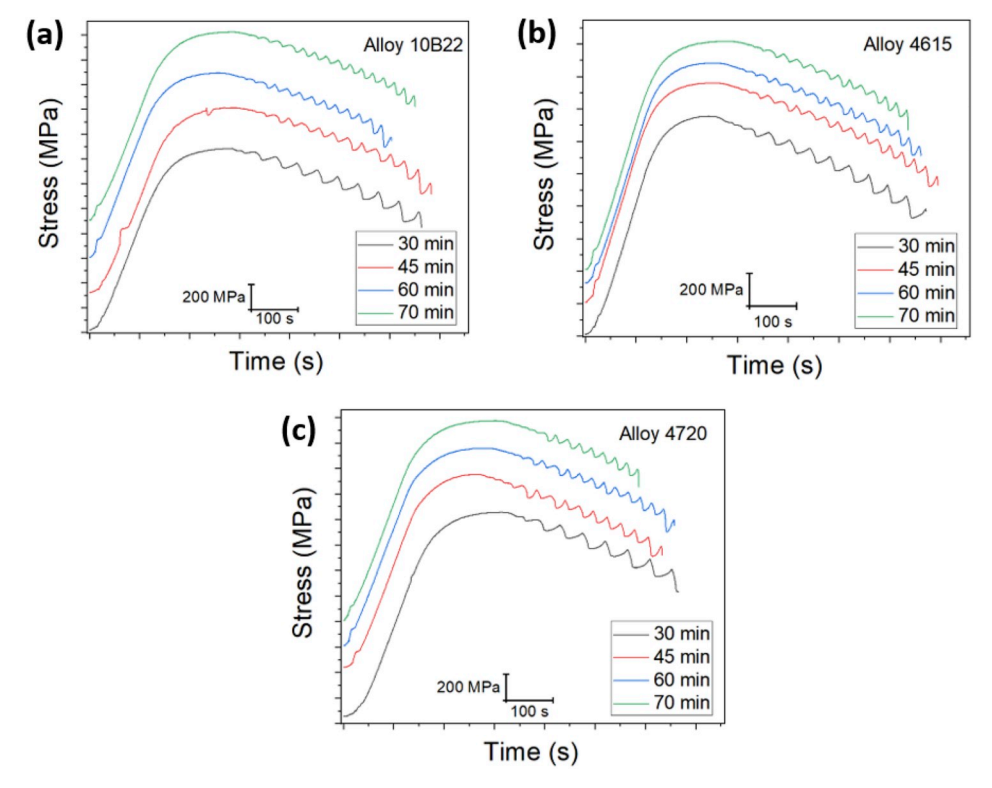


Fig. 7. Engineering stress vs. time graphs. Here serrations can be observed for alloys, (a) 10B22, (b) 4615, and (c) 4720.

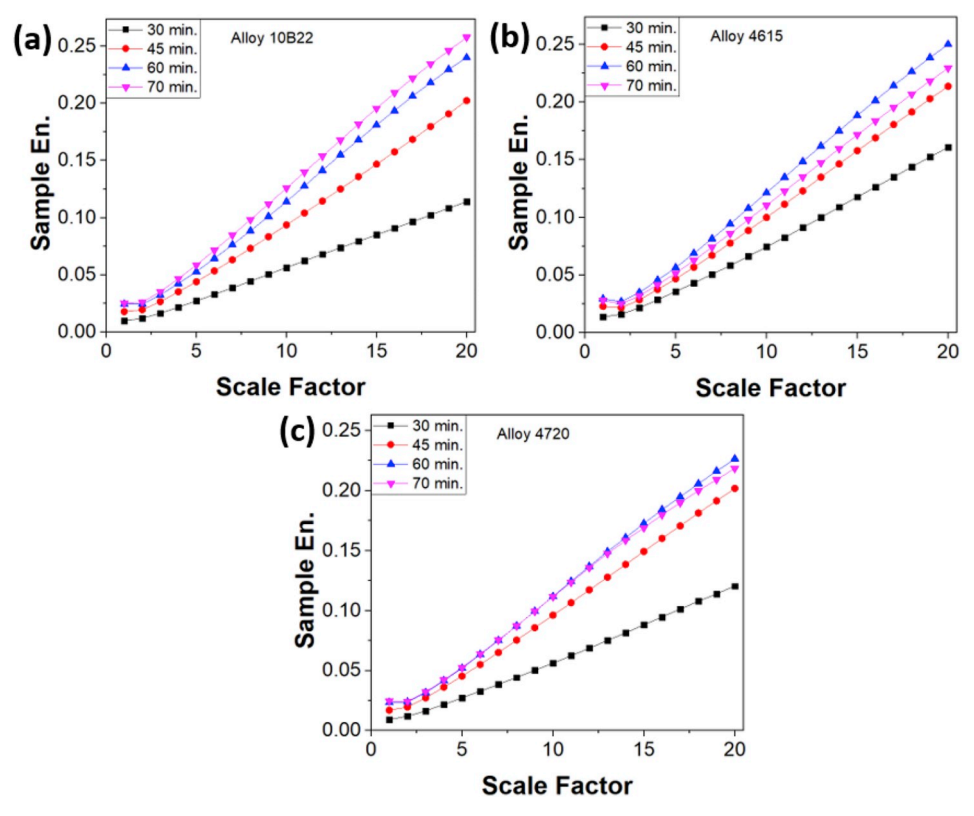


Fig. 8. RCMSE of the serrated flow at different heating times for alloys, (a) 10B22, (b) 4615, and (c) 4720.

will be accompanied by a larger number of interstitials that are available to participate in Snoek ordering and interstitial-dislocation line interactions.

In addition to carbon, there are other factors that may contribute to the serrated flow such as stacking faults and substitutional solutes. For instance, the stacking faults partly contribute to the manifestation of dynamic strain aging (DSA) by interacting with substitutional solute atoms in the matrix that have low stacking fault energy [72]. In this scenario, the solute atoms initially diffuse along dislocations until they encounter a stacking fault, where they obstruct their motion [39].

Finally, the greater total elongation that was exhibited by alloy 4615, as compared to alloys 4720 and 10B22, may be a consequence of

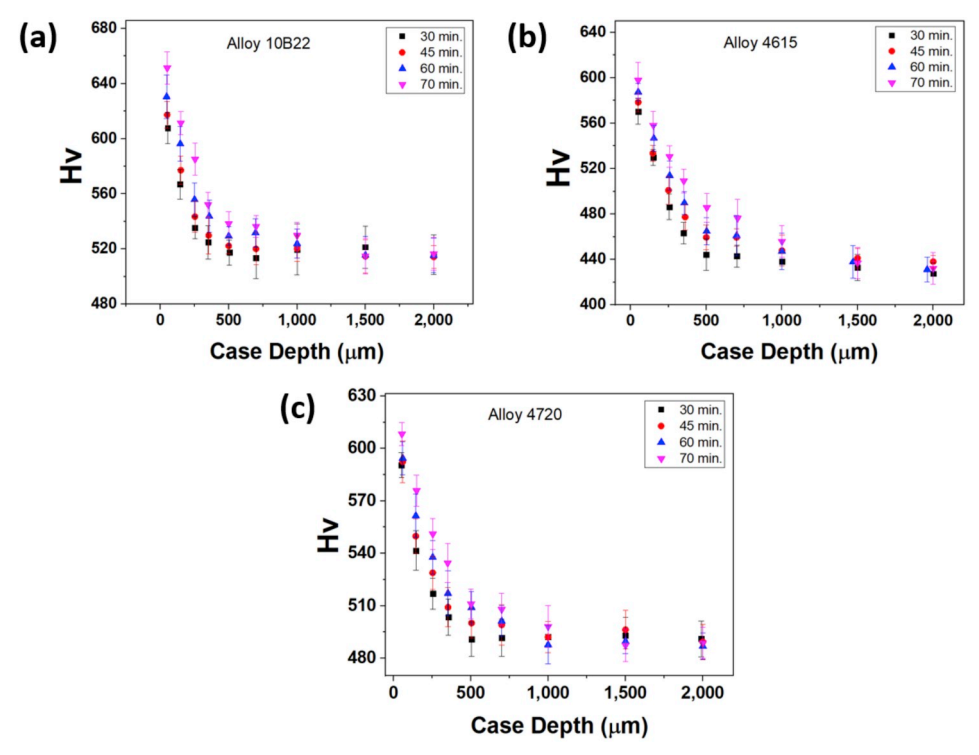


Fig. 9. Plot of hardness vs. case depth for low-carbon steel alloys, (a) 10B22, (b) 4615, and (c) 4720.

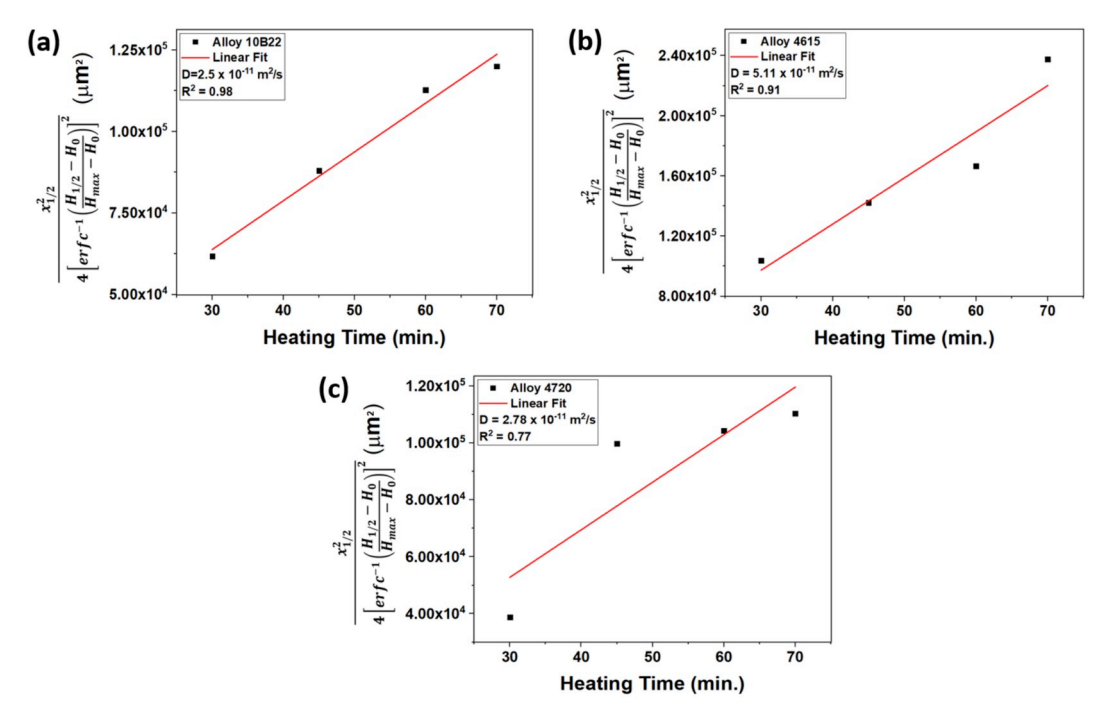


Fig. 10. Dt plotted vs. heating time for alloys, (a) 10B22, (b) 4615, and (c) 4720.

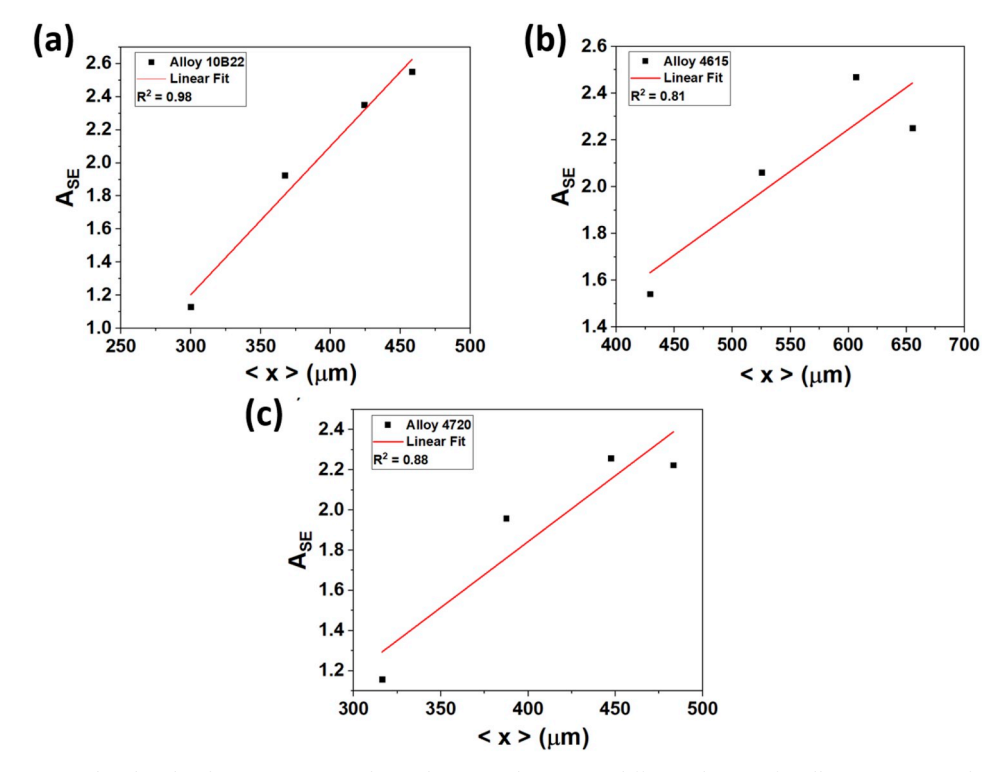


Fig. 11. Plot of the area enclosed under the RCMSE curve (denoted A_{SE}) vs. the average diffusion distance for alloys, (a) 10B22, (b) 4615, and (c) 4720.

its larger Mo content. Here, the Mo segregates at dislocation slip bands, which alleviates the local strain concentrations [38]. As a result, the local strain dynamic recovery occurs, which leads to improved tensile ductility during tension.

5.2. Complexity modeling and analysis of the serration behavior

The stress drops, as shown in Fig. 6(a)-(c), generally occurred below the local averaged level of stress, which is indicative of Type-C serrations [14,65]. Since Type-C serrations are believed to be less spatially

correlated [33], as compared to say, Types-A and B serrations, it suggests that the locking events occurring in these alloys during tension take place in a more random nature. The above statement is supported by the fact that the sample-entropy values in the present work were similar to those reported in Ref. [32] for Type-C serrations. For a visual depiction of these three types of serrations, please see Fig. 13 [14,18,65]. As displayed in the figure, the Type-C serrations exhibit a sharp decrease below the general level of stress. On the other hand, the Type-B serrated flow exhibits rapid fluctuations that occur around the local averaged stress curve. Finally, Type-A serrations display the

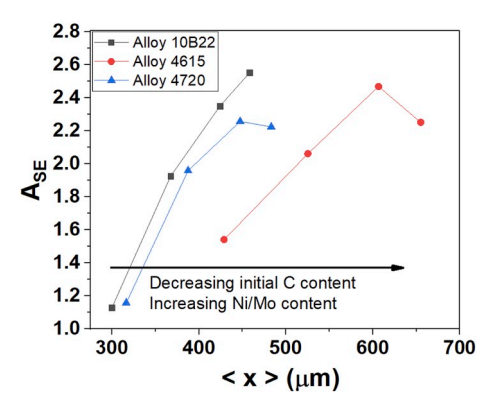


Fig. 12. The area enclosed under the RCMSE curve (denoted A_{SE}) vs. the average diffusion distance for all three alloys.

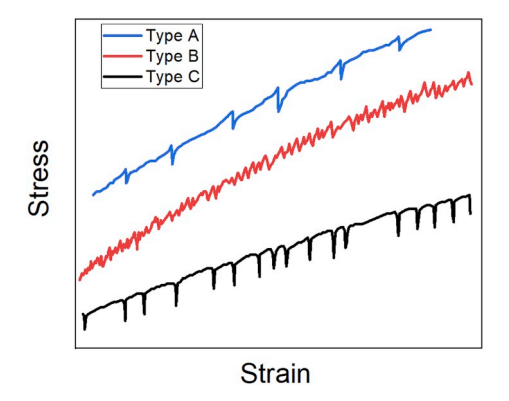


Fig. 13. Types A, B, and C serrations [14,18,65].

periodic behavior in which the oscillations rise abruptly and then drop below the local averaged stress curve [65].

Fig. 8(a)-(c) suggest that the complexity of the serrations increased, in all cases, with respect to the scale factor. This continual increase in the complexity at higher scale factors is symptomatic of an increase in the variety of possible locking interactions that can occur during tension. This rise also indicates that the serrations exhibit the dynamical behavior that consists of more complex structures across a greater range of spatial and temporal scales. Furthermore, this increase is due in part to the fact that carbon can interact with a wider variety of dislocations, as compared to other atoms in the matrix.

Moreover, the sample entropy, on average, was found to increase with respect to the heating time, which can be seen in Fig. 8(a)-(c). As these specimens are heated longer, carbon diffuses further into the matrix. As discussed above, the sample entropy corresponds to the level of spatial correlations that occur between locking events. Therefore, as the carbon content in a region of the matrix increases, there is a higher probability that locking events leading to serrations will be closer to one another. Consequently, this trend leads to stress-drop events in which the locking events are more spatially correlated. Therefore, an increase in carbon atoms, via annealing, will lead to a larger number and greater variety of interactions that will lead to more complicated dynamics during the serrated flow [see Fig. 8(a)-(c)].

As can be seen in Fig. 12, the sample entropy was characteristically higher for alloy 4615, which had a lower initial carbon content. This trend was especially pronounced for heating times of 30 and 45 min. Furthermore, the relatively lower carbon content in the same alloy was also reflected by the results of the Vickers hardness tests, [displayed in Fig. 9(a)-(c)] where the hardness curves were lower across all heating times, as compared to alloys 4720 and 10B22. As can be surmised from Table 1 and Fig. 12, the higher sample-entropy values, despite the lower initial carbon content, may arise from the greater nickel and/or molybdenum content in the alloy. As discussed previously, the

substitutional solute atoms can provide an obstacle for stacking faults, leading to DSA [39]. Therefore, an increase in the concentrations of Ni and Mo in the matrix should, in theory, result in a greater number of interactions during the DSA, which corresponds to more complex dynamics underlying the serrated flow. Also, the curve for the alloy, 4615, had the highest average diffusion distance and average complexity for heating times < 70 min, as compared to the other alloys. Here, the increased carbon migration in the alloy, 4615, may be caused by the higher chemical potential arising from a lower initial carbon content in the as-received state (please see Table 1).

As discussed above, the diffusion coefficient for the alloy, 4615 $(5.11 \times 10^{-11} \, \text{m}^2/\text{s})$, was twice as high as the one for the other two alloys. Typically, a higher diffusion coefficient means that more carbon will diffuse into the alloy for a given heating time. As discussed earlier, as more carbon diffuses into the matrix, there will be a greater number of interstitial defects that can create tetragonal distortions in the matrix. Consequently, a greater number of tetragonal distortions will be able to interact with more edge and screw dislocations, leading to more complex dynamics during the serrated flow. Therefore, the higher complexity values for the alloy, 4615, as compared to alloys, 10B22 and 4720, is a consequence of the higher diffusion rate in the alloy.

A drop in the sample entropy curves for alloys 4615 and 4720, which were heated for 70 min. [see Fig. 8(a)-(c)], can be explained as follows. After a heating time of 60 min, the alloy becomes saturated with carbon impurities to a point that they cannot participate in as many complex interactions that influence serrations. Furthermore, impurities may cluster and become sinks for other interstitials, thereby decreasing the amount of dislocation locking that occurs during tension. This clustering, which is thought to occur in all of the alloys, may be caused by elements such as nickel or molybdenum that are contained in the matrix.

6. Conclusions

The present work studied the serrated-flow behavior in three carburized steels undergoing room-temperature tension experiments with an applied strain rate of 2×10^{-4} s⁻¹ after annealing at 885 °C for time intervals ranging from 30 to 70 min. The following conclusions were inferred from the experimental outcomes. The carburized steel alloys were found to be relatively ductile, as revealed by the SEM images of fractured surfaces. The complexity of the serrated flow was found to increase with the carburization time, and, consequently, the carbon content of the alloy. Importantly, the sample entropy was found to increase with respect to the mean-squares displacement of carbon into the alloy. This increase in the complexity with the increasing carbon content is thought to be related to the more varied ways that carbon can interact with dislocations, as compared to other solute atoms in the matrix. Finally, the results suggest that an increase in the amount of the substitutional point defects in the alloy lead to a higher number of interactions with stacking faults during tension, resulting in more complex dynamics during the serrated flow.

Author contributions

All authors assisted with the work presented in the manuscript. B.C. and R.Y. performed the high-energy XRD. B.C. and J.D.V. prepared the samples and performed the tension testing while J.B. performed the Vickers-hardness tests. The analysis of the stress-time and Vickers-hardness data was performed by J.B. and X.X. J.B., B.C., P.K.L., and S.J.Z. composed the main body of the document while all authors deliberated the results and remarked on the manuscript over the course of its preparation.

Competing financial interests

The authors declare that they have no competing financial interests.

Correspondence and requests for materials should be addressed to P. K. L. (pliaw@utk.edu)

Data availability

The raw/processed data required to reproduce these findings cannot be shared at this time due to legal or ethical reasons.

Acknowledgements

Funding: The authors are grateful to the financial supports from the Columbus McKinnon Corporation, Lab-Directed Research and Development (LDRD) at the Oak Ridge National Laboratory, and the Center for Materials Processing at The University of Tennessee. X. X. and P. K. L. are extremely thankful for the gracious funding from the U.S. Department of Energy (DOE) Office of Fossil Energy, the National Science Foundation (DMR-1611180, and DMR-1809640), and the National Energy Technology Laboratory (NETL) (DE-FE0008855, DE-FE-0024054, and DE-FE-0011194), with program managers Drs. D. Farkas, V. Cedro, S. Markovich, G. Shiflet, J. Mullen, and R. Dunts. B. C. and P. K. L. would like to acknowledge the financial support of Columbus McKinnon. The current project utilized resources available at the Advanced Photon Source, a U.S. Department of Energy (DOE) Office of Science User Facility operated for the DOE Office of Science by the Argonne National Laboratory under Contract No. DE-AC02-06CH11357.

Appendix A. Supplementary data

Supplementary data to this article can be found online at https://doi.org/10.1016/j.msea.2019.02.096.

References

- J. Antonaglia, X. Xie, G. Schwarz, M. Wraith, J. Qiao, Y. Zhang, P.K. Liaw, J.T. Uhl, K.A. Dahmen, Tuned critical avalanche scaling in bulk metallic glasses, Sci. Rep. 4 (2014).
- [2] J.W. Qiao, Y. Zhang, P.K. Liaw, Serrated flow kinetics in a Zr-based bulk metallic glass, Intermetallics 18 (2010) 2057–2064.
- [3] J.W. Qiao, H.L. Jia, Y. Zhang, P.K. Liaw, L.F. Li, Multi-step shear banding for bulk metallic glasses at ambient and cryogenic temperatures, Mater. Chem. Phys. 136 (155501) (2012) 1–5.
- [4] J. Antonaglia, W.J. Wright, X. Gu, R.R. Byer, T.C. Hufnagel, M. LeBlanc, J.T. Uhl, K.A. Dahmen, Bulk metallic glasses deform via slip avalanches, Phys. Rev. Lett. 112 (155501) (2014) 1–5.
- [5] W.J. Wright, Y. Liu, X. Gu, K.D.V. Ness, S.L. Robare, X. Liu, J. Antonaglia, M. LeBlanc, J.T. Uhl, T.C. Hufnagel, K.A. Dahmen, Experimental evidence for both progressive and simultaneous shear banding during quasistatic compression of a bulk metallic glass, J. Appl. Phys. 119 (084908) (2016) 1–6.
- [6] J.J. Li, Z. Wang, J.W. Qiao, Power-law scaling between mean stress drops and strain rates in bulk metallic glasses, Mater. Des. 99 (2016) 427–432.
- [7] C.A. Schuh, T.C. Hufnagel, U. Ramamurty, Overview No.144 mechanical behavior of amorphous alloys, Acta Mater. 55 (12) (2007) 4067–4109.
- [8] F. Haag, D. Beitelschmidt, J. Eckert, K. Durst, Influences of residual stresses on the serrated flow in bulk metallic glass under elastostatic four-point bending. A nanoindentation and atomic force microscopy study, Acta Mater. 70 (2014) 188–197.
- [9] B.A. Sun, S. Pauly, J. Tan, M. Stoica, W.H. Wang, U. Kuhn, J. Eckert, Serrated flow and stick-slip deformation dynamics in the presence of shear-band interactions for a Zr-based metallic glass, Acta Mater. 60 (10) (2012) 4160–4171.
- [10] R. Maass, D. Klaumuenzer, J.F. Loffler, Propagation dynamics of individual shear bands during inhomogeneous flow in a Zr-based bulk metallic glass, Acta Mater. 59 (8) (2011) 3205–3213.
- [11] G. Wang, K.C. Chan, L. Xia, P. Yu, J. Shen, W.H. Wang, Self-organized intermittent plastic flow in bulk metallic glasses, Acta Mater. 57 (20) (2009) 6146–6155.
- [12] W.H. Jiang, F.E. Pinkerton, M. Atzmon, Mechanical behavior of shear bands and the effect of their relaxation in a rolled amorphous Al-based alloy, Acta Mater. 53 (12) (2005) 3469–3477.
- [13] C.A. Schuh, T.G. Nieh, A nanoindentation study of serrated flow in bulk metallic glasses, Acta Mater. 51 (1) (2003) 87–99.
- [14] Y. Zhang, J.P. Liu, S.Y. Chen, X. Xie, P.K. Liaw, K.A. Dahmen, J.W. Qiao, Y.L. Wang, Serration and noise behaviors in materials, Prog. Mater. Sci. 90 (2017) 358–460.
- [15] X. Xie, Y.-C. Lo, Y. Tong, J. Qiao, G. Wang, S. Ogata, H. Qi, K.A. Dahmen, Y. Gao, P.K. Liaw, Origin of serrated flow in bulk metallic glasses, J. Mech. Phys. Solids 124 (2019) 634–642.
- [16] R. Rashidi, M. Malekan, Y. Hamishebahar, Serration dynamics in the presence of

- chemical heterogeneities for a Cu-Zr based bulk metallic glass, J. Alloy. Comp. 775 (2019) 298–303.
- [17] S. Chen, X. Xie, B.L. Chen, J.W. Qiao, Y. Zhang, Y. Ren, K.A. Dahmen, P.K. Liaw, Effects of temperature on serrated flows of Al_{0.5}CoCrCuFeNi high-entropy alloy, J. Occup. Med. 67 (10) (2015) 2314–2320.
- [18] R. Carroll, C. Lee, C.-W. Tsai, J.-W. Yeh, J. Antonaglia, B.A.W. Brinkman, M. LeBlanc, X. Xie, S. Chen, P.K. Liaw, K.A. Dahmen, Experiments and model for serration statistics in low entropy, medium-entropy, and high-entropy alloys, Sci. Rep. 5 (16997) (2015).
- [19] S.Y. Chen, X. Yang, K.A. Dahmen, P.K. Liaw, Y. Zhang, Microstructures and crackling noise of Al_xNbTiMoV high entropy alloys, Entropy 16 (2014) 870–884.
- [20] S. Chen, L. Yu, J. Ren, X. Xie, X. Li, Y. Xu, G. Zhao, P. Li, F. Yang, Y. Ren, P.K. Liaw, Self-similar random process and chaotic behavior in serrated flow of high entropy alloys, Sci. Rep. 6 (2016) 29798.
- [21] S. Chen, X. Xie, W. Li, R. Feng, B. Chen, J. Qiao, Y. Ren, Y. Zhang, K.A. Dahmen, P.K. Liaw, Temperature effects on the serrated behavior of an Al_{0.5}CoCrCuFeNi high-entropy alloy, Mater. Chem. Phys. 210 (2018) 20–28.
- [22] X.X. Guo, X. Xie, J.L. Ren, M. Laktionova, E. Tabachnikova, L.P. Yu, W.-S. Cheung, K.A. Dahmen, P.K. Liaw, Plastic dynamics of the Al_{0.5}CoGrCuFeNi high entropy alloy at cryogenic temperatures: Jerky flow, stair-like fluctuation, scaling behavior, and non-chaotic state, Appl. Phys. Lett. 111 (25) (2017).
- [23] H.Y. Diao, R. Feng, K.A. Dahmen, P.K. Liaw, Fundamental deformation behavior in high-entropy alloys: an overview, Curr. Opin. Solid State Mater. Sci. 21 (5) (2017) 252–266
- [24] S. Niu, H. Kou, Y. Zhang, J. Wang, J. Li, The characteristics of serration in Al_{0.5}CoCrFeNi high entropy alloy, Mater. Sci. Eng., A 702 (2017) 96–103.
- [25] M. Komarasamy, K. Alagarsamy, R.S. Mishra, Serration behavior and negative strain rate sensitivity of Al_{0.1}CoCrFeNi high entropy alloy, Intermetallics 84 (2017) 20–24.
- [26] B.F. Wang, A. Fu, X.X. Huang, B. Liu, Y. Liu, Z.Z. Li, X. Zan, Mechanical properties and microstructure of the CoCrFeMnNi high entropy alloy under high strain rate compression, J. Mater. Eng. Perform. 25 (7) (2016) 2985–2992.
- [27] Y. Zhang, W.H. Wang, P.K. Liaw, G. Wang, J.W. Qiao, Serration and noise behavior in advanced materials, J. Iron Steel Res. Int. 23 (1) (2016) 1-1.
- [28] J. Antonaglia, X. Xie, Z. Tang, C.W. Tsai, J.W. Qiao, Y. Zhang, M.O. Laktionova, E.D. Tabachnikova, J.W. Yeh, O.N. Senkov, M.C. Gao, J.T. Uhl, P.K. Liaw, K.A. Dahmen, Temperature effects on deformation and serration behavior of highentropy alloys (HEAs), J. Mater. 66 (10) (2014) 2002–2008.
- [29] S.Y. Chen, W.D. Li, X. Xie, J. Brechtl, B.L. Chen, P.Z. Li, G.F. Zhao, F.Q. Yang, J.W. Qiao, P.K. Liaw, Nanoscale serration and creep characteristics of Al_{0.5}CoCrCuFeNi high-entropy alloys, J. Alloy. Comp. 752 (2018) 464–475.
 [30] J. Brechtl, S.Y. Chen, X. Xie, Y. Ren, J.W. Qiao, P.K. Liaw, S.J. Zinkle, Towards a
- [30] J. Brechtl, S.Y. Chen, X. Xie, Y. Ren, J.W. Qiao, P.K. Liaw, S.J. Zinkle, Towards a greater understanding of serrated flows in an Al-containing high-entropy-based alloy. Int. J. Plast. 115 (2019) 71–92.
- [31] A. Sarkar, A. Chatterjee, P. Barat, P. Mukherjee, Comparative study of the Portevin-Le Chatelier effect in interstitial and substitutional alloy, Mater. Sci. Eng. 459 (2007) 361–365.
- [32] A. Sarkar, P. Barat, P. Mukherjee, Multiscale entropy analysis of the Portevin-Le Chatelier effect in an Al-2.5%Mg alloy, Fractals 18 (3) (2009) 319–325.
- [33] A. Sarkar, S.A. Maloy, K.L. Murty, Investigation of Portevin-LeChatelier effect in HT-9 steel, Mater. Sci. Eng. 631 (2015) 120–125.
- [34] A. Iliopoulous, N.S. Nikolaidis, E.C. Aifantis, Analysis of serrations and shear bands fractality in UFGs, J. Mech. Behav. Mater. 24 (1–2) (2015) 1–9.
- [35] J.T. Uhl, S. Pathak, D. Schorlemmer, X. Liu, R. Swindeman, B.A.W. Brinkman, M. LeBlanc, G. Tsekenis, N. Friedman, R. Behringer, D. Denisov, P. Schall, X. Gu, W.J. Wright, T. Hufnagel, A. Jennings, J.R. Greer, P.K. Liaw, T. Becker, G. Dresen, K.A. Dahmen, Universal quake statistics: from compressed nanocrystals to earthquakes, Sci. Rep. 5 (2015).
- [36] A.F. Rowcliffe, S.J. Zinkle, D.T. Hoelzer, Effect of strain rate on the tensile properties of unirradiated and irradiated V–4Cr–4Ti, J. Nucl. Mater. 283–287 (2000) 508–512
- [37] N. Friedman, A.T. Jennings, G. Tsekenis, J.-Y. Kim, M. Tao, J.T. Uhl, J.R. Greer, K.A. Dahmen, Statistics of dislocation slip avalanches in nanosized single crystals show tuned critical behavior predicted by a simple mean field model, Phys. Rev. Lett. 109 (095507) (2012) 1–5.
- [38] Y.Y. Hong, S.L. Li, H.J. Li, J. Li, G.G. Sun, Y.D. Wang, Development of intergranular residual stress and its implication to mechanical behaviors at elevated temperatures in AL6XN austenitic stainless steel, Metall. Mater. Trans. A-Phys. Metall. Mater. Sci. 49A (8) (2018) 3237–3246.
- [39] C. Tian, C. Cui, L. Xu, Y. Gu, X. Sun, Dynamic strain aging in a newly developed Ni–Co-base superalloy with low stacking fault energy, J. Mater. Sci. Technol. 29 (9) (2013) 873–878.
- [40] A.S. Alomari, N. Kumar, K.L. Murty, Enhanced ductility in dynamic strain aging regime in a Fe-25Ni-20Cr austenitic stainless steel, Mater. Sci. Eng. A-Struct. Mater. Prop. Microstruct. Process. 729 (2018) 157–160.
- [41] M. Koyama, T. Sawaguchi, K. Tsuzaki, Overview of dynamic strain aging and associated phenomena in Fe-Mn-C austenitic steels, ISIJ Int. 58 (8) (2018) 1383–1395.
- [42] P. Lan, J.Q. Zhang, Serrated Flow and dynamic strain aging in Fe-Mn-C TWIP steel, Metall. Mater. Trans. A-Phys. Metall. Mater. Sci. 49A (1) (2018) 147–161.
- [43] X.D. Bian, F.P. Yuan, X.L. Wu, Correlation between strain rate sensitivity and characteristics of Portevin-LeChatelier bands in a twinning-induced plasticity steel, Mater. Sci. Eng. A-Struct. Mater. Prop. Microstruct. Process. 696 (2017) 220–227.
- [44] N.C.S. Srinivas, P. Verma, V. Singh, Dynamic strain ageing behaviour of modified 9Cr-1Mo steel under monotonic and cyclic loading, Procedia Engineering 184 (2017) 765–772.

- [45] A.F. Rowcliffe, S.J. Zinkle, D.T. Hoelzer, Effect of strain rate on the tensile properties of unirradiated and irradiated V-4Cr-4Ti, J. Nucl. Mater. 283 (2000) 508–512.
- [46] Q.S. Li, Y.Z. Shen, P.C. Han, Iop, Serrated Flow Behavior of Aisi 316l Austenitic Stainless Steel for Nuclear Reactors, 3rd Annual International Workshop on Materials Science and Engineering, Iop Publishing Ltd, Bristol, 2017.
- [47] Y.C. Lin, H. Yang, Y.C. Xin, C.Z. Li, Effects of initial microstructures on serrated flow features and fracture mechanisms of a nickel-based superalloy, Mater. Char. 144 (2018) 9–21.
- [48] L. Yuan, R. Hu, J.S. Li, X.Y. Gao, X.Q. Zhang, Y.A. Yang, New insights into serrated flow in Pt2Mo-type superlattice strengthened Ni-Cr-Mo alloy at room temperature, Mater. Lett. 163 (2016) 94–97.
- [49] A. Chiba, X.G. Li, M.S. Kim, High work-hardening rate and deformation twinning of Co-Ni-based superalloy at elevated temperatures, Philos. Mag. A-Phys. Condens. Matter Struct. Defect Mech. Prop. 79 (7) (1999) 1533–1554.
- [50] J.K. Sung, M.S. Kim, W.Y. Kim, A. Chiba, Effect of grain size on mechanical properties of single phase Co-NI-Cr-Mo based superalloy, in: Z.Y. Zhong, H. Saka, T.H. Kim, E.A. Holm, Y.F. Han, X.S. Xie (Eds.), Pricm 5: the Fifth Pacific Rim International Conference on Advanced Materials and Processing, Pts 1-5, Trans Tech Publications Ltd, Zurich-Uetikon, 2005, pp. 631–634.
- [51] A. Humeau-Heurtier, The multiscale entropy algorithm and its variants: a review, Entropy 17 (2015) 3110–3123.
- [52] M. Costa, A.L. Goldberger, C.K. Peng, Multiscale entropy analysis of complex physiologic time series, Phys. Rev. Lett. 89 (6) (2002) 068102.
- [53] S.-D. Wu, C.-W. Wu, S.-G. Lin, C.-C. Wang, K.-Y. Lee, Time series analysis using composite multiscale entropy, Entropy 15 (2013) 1069–1084.
- [54] M. Costa, A.L. Goldberger, C.K. Peng, Multiscale entropy analysis of biological signals, Phys. Rev. 71 (2) (2005) 021906.
- [55] M. Costa, C.-K. Peng, A.L. Goldberger, J.M. Hausdorff, Multiscale entropy analysis of human gait dynamics, Physica A 330 (2003) 53–60.
- [56] S.-D. Wu, C.-W. Wu, S.-G. Lin, K.-Y. Lee, C.-K. Peng, Analysis of complex time series using refined composite multiscale entropy, Phys. Lett. 378 (2014) 1369–1374.
- [57] J. Xia, P. Shang, Multiscale entropy analysis of financial time series, Fluctuation Noise Lett. 11 (4) (2012) 1–12.
- [58] M.C. Chang, C.K. Peng, H.E. Stanley, Emergence of dynamical complexity related to human heart rate variability, Phys. Rev. 90 (6) (2014) 5.

- [59] W. Cai, W.D. Nix, Imperfections in Crystalline Solids, Cambridge University Press, Cambridge, 2016.
- [60] A.W. Cochardt, G. Schoek, H. Wiedersich, Interaction between dislocations and interstitial atoms in body-centered cubic metals, Acta Metall. 3 (1955) 533–537.
- [61] A. E384-16, Standard test method for microindentation hardness of materials, West Conshohocken, PA, www.astm.org, (2016).
- [62] J. Brechtl, X. Xie, P.K. Liaw, S.J. Zinkle, Complexity modeling and analysis of chaos and other fluctuating phenomena, Chaos, Solitons & Fractals 116 (2018) 166–175.
- [63] S.M. Pincus, Approximate entropy as a measure of system complexity, Proc. Natl. Acad. Sci. 88 (1991) 2297–2301.
- [64] S. Reulecke, S. Charleston-Villalobos, A. Voss, R. Gonzalez-Camarena, J.A. Gonzalez-Hermosillo, M.J. Gaitan-Gonzalez, G. Hernandez-Pacheco, R. Schroeder, T. Aljama-Corrales, Temporal analysis of cardiovascular and respiratory complexity by multiscale entropy based on symbolic dynamics, IEEE J. Biomed. Health Inform. 22 (4) (2018) 1046–1058.
- [65] P. Rodriguez, Serrated plastic flow, Bull. Mater. Sci. 6 (4) (1984) 653-663.
- [66] J. Baillieux, D. Poquillon, B. Malard, Observation using synchrotron X-ray diffraction of the crystallographic evolution of α-titanium after oxygen diffusion, Phil. Mag. Lett. 95 (5) (2015) 245–252.
- [67] E.A. Brandes, G.B. Brook, Smithells Metals Reference, Book, Oxford, 1992.
- [68] A. Crespo, D. Álvarez, G.C. Gutiérrez-Tobal, F. Vaquerizo-Villar, V. Barroso-García, M.L. Alonso-Álvarez, J. Terán-Santos, R. Hornero, F.d. Campo, Multiscale entropy analysis of unattended oximetric recordings to assist in the screening of paediatric sleep apnoea at home, Entropy 19 (6) (2017) 284.
- [69] G.K. Williamson, R.E. Smallman, X-ray evidence for the interstitial position of carbon in α-iron, Acta Crystallogr. 6 (1953) 361–362.
- [70] J. Snoek, Effect of small quantities of carbon and nitrogen on the elastic and plastic properties of iron, Acta Metall. 7 (1959) 628–631.
- [71] D.V. Wilson, B. Russell, Stress induced ordering and strain-ageing in low carbon steels, Acta Metall. 7 (1959) 628–631.
- [72] Y. Cao, C. Zhang, C. Zhang, H. Di, G. Huang, Q. Liu, Influence of dynamic strain aging on the mechanical properties and microstructural evolution for Alloy 800H during hot deformation, Mater. Sci. Eng., A 724 (2018) 37–44.
- [73] Brechtl, X. Xie, P.K. Liaw, Investigation of chaos and memory effects in the Bonhoeffer-van der Pol oscillator with a non-ideal capacitor, Commun. Nonlinear Sci. Numer. Simul. 73 (2019) 195–216.